Geophys. J. Int. (1997) **128,** 505–521

Finite-difference modelling of magnetotelluric fields in two-dimensional anisotropic media

Josef Pek and Tomáš Verner
Geophysical Institute, Academy of Sciences of the Czech Republic, Bočni II/1401, 14131 *Prague* 4–*Spořilov, Czech Republic*

Accepted 1996 October 10. Received 1996 August 5; in original form 1995 December 6

SUMMARY

An algorithm for the numerical modelling of magnetotelluric fields in 2-D generally anisotropic block structures is presented. Electrical properties of the individual homogeneous blocks are described by an arbitrary symmetric and positive-definite conductivity tensor. The problem leads to a coupled system of partial differential equations for the strike-parallel components of the electromagnetic field, E_x and H_x. These equations are numerically approximated by the finite-difference (FD) method, making use of the integro-interpolation approach. As the magnetic component H_x is constant in the non-conductive air, only equations for the electric mode are approximated within the air layer. The system of linear difference equations, resulting from the FD approximation, can be arranged in such a way that its matrix is symmetric and band-limited, and can be solved, for not too large models, by Gaussian elimination. The algorithm is applied to model situations which demonstrate some non-trivial phenomena caused by electrical anisotropy. In particular, the effect of 2-D anisotropy on the relation between magnetotelluric impedances and induction arrows is studied in detail.

Key words: 2-D structures, electrical anisotropy, finite-difference method, magnetotelluric sounding

1 INTRODUCTION

Recently, several attempts to interpret magnetotelluric data have appeared in which large electrical anisotropy of deep geoelectrical structures plays a substantial role, 'large' referring to as much as several orders of magnitude in terms of the anisotropy ratio $\lambda = \rho_{max}/\rho_{min}$. A typical example is data from around the deep borehole KTB in Oberpfalz (Germany), where a highly anisotropic structure of regional extent (λ as high as 10^3) is proposed by several authors (e.g. Tauber 1993; Eisel 1994; Červ, Pek & Praus 1994) to explain a large anisotropy of the magnetotelluric curves and a systematic discrepancy between the magnetotelluric principal directions and those indicated by the induction arrows. As a physical source of this large anisotropy, a collective effect of narrow, nearly vertical graphitized cataclastic zones, detected in this region in near-surface structures (e.g. Stoll 1989) as well as on the KTB borehole log (e.g. Winter 1994), is hypothesized (Eisel 1994), although other physical mechanisms, specifically the effect of fluids and sulphides, have to be considered (Tauber 1993; Winter 1994). There are more examples of large anisotropies interpreted at various depths of the crust or upper mantle, for example in Tezkan (1988) for the data from the contact zone of the Rhenohercynikum and the Northern Phyllite Zone, Germany, in Tezkan, Červ & Pek (1992) from the contact of the Rhine-Graben and Black Forest, Germany, in Eisel & Bahr (1993) and Jones, Groom & Kurtz (1993) for the BC87 data set from British Columbia, Canada, and in Kurtz *et al.* (1993) for the data from the Kapuskasing Uplift, Ontario, Canada, to mention a few. The latter paper reports several references related to the subject.

Methods currently used for modelling the effects of the electrical anisotropy on the magnetotelluric data are mostly based on rather oversimplified assumptions—either 1-D approximations of the Earth's structure employed on the local scale, or 2-D models with different conductivities for the E and H polarization modes—thus constraining the anisotropy in such a way that the conductivity tensor must reduce to the diagonal form just in the strike-bound coordinate system. A physically more plausible model of the electrical macroanisotropy, used in a series of interpretations (e.g. Tezkan 1988; Tezkan *et al.* 1992; Eisel 1994), and based on stacking alternately conductive and non-conductive dykes, is subject to the same constraint. Unless powerful 3-D modelling tools are used, only structures with dykes parallel to the strike of the model can be managed. It is clear that the above 2-D approximations of the electrical anisotropy do remain within the reach of 2-D algorithms currently used to model 2-D

isotropic geoelectrical structures, and they do not allow some features, which are intuitively expected to occur in models with general anisotropy, to be verified and quantitatively analysed.

Although a sufficiently general finite-element algorithm for the modelling of magnetotelluric fields in 2-D structures with genuine anisotropy was published 20 years ago (Reddy & Rankin 1975), it has not yet been used in practical applications, as far as we know. Since then, articles dealing with anisotropy in multidimensional geoelectrical structures have appeared only sporadically, and only now does the question seem to be attracting more attention again.

In Saraf, Negi & Červ (1986) the finite-difference modelling algorithm for the H-polarization mode was generalized to allow for structures with different conductivities in the horizontal and vertical directions. Using a Rayleigh FFT technique, Osella & Martinelli (1993) could model the magnetotelluric response of 2-D anisotropic structures with smoothly varying layer boundaries, including models with a smooth topography. In their algorithm, however, the conductivity tensor is supposed to be diagonal in the strike-bound coordinate system. The first 3-D modelling results for anisotropic structures were presented by Xiong (1989), who used the integral equation technique to compute the electromagnetic field of a 3-D body embedded in a stratified anisotropic earth.

Recently, Schmucker (1994a,b) presented a 2-D thin-sheet modelling algorithm which allows the bimodal induction in a 2-D thin sheet underlain by an arbitrary layered anisotropic half-space to be calculated. In Grubert (1994), the original analytic H-polarization solution of the classical problem of a vertical contact of two quarter-spaces (d'Erceville & Kunetz 1962) has been generalized to anisotropic quarter-spaces with dipping anisotropy. With Weidelt's (1994) extension of the finite-difference 3-D forward modelling algorithm of Mackie, Madden & Wannamaker (1993) to generally anisotropic 3-D media, the modelling of anisotropic geoelectrical structures seems to reach its culmination.

Although a general 3-D algorithm is now available to model anisotropic geoelectrical structures, we still consider relatively simple 2-D modelling approaches to be quite useful in many situations. The main aim of this contribution is to present a new version of a numerical algorithm which makes it possible to model magnetotelluric fields in 2-D structures containing quite generally anisotropic subdomains. The algorithm is based on the finite-difference approximation of a coupled system of second-order partial differential equations, which are a generalization of the Helmholtz equations, well known from 2-D isotropic studies. Since many of the general ideas of the present method have been adopted from Reddy & Rankin (1975), we do not pretend to have developed a totally new algorithm, we rather consider our version a 'come back' of an old approach with a few new features, in particular as regards the general character of the anisotropy and the construction of the finite-difference scheme.

2 FORMULATION OF THE PROBLEM

We assume a traditional 2-D geoelectric model with its structural strike parallel to the x-axis of the Cartesian coordinate system. The z-axis is positive downwards. The model consists of a finite system of homogeneous, but in general anisotropic, 2-D blocks. 2-D inhomogeneities are confined to a finite region within the model. Outside this region, the structure merges into its anisotropic layered background, which can be in general different for either side of the model. The earth's surface is assumed to be planar (no topography is considered here) and to coincide with the coordinate plane $z = 0$. Above the surface a perfectly insulating air layer is assumed. The primary electromagnetic field is modelled by a monochromatic electromagnetic plane wave (angular frequency $\omega = 2\pi/T$, with T being the period) propagating perpendicularly to the earth's surface from sources located at $z = -\infty$.

In the quasi-stationary approximation, the governing equations for the electromagnetic field are Maxwell's equations in the form

$$\nabla \times \mathbf{E} = i\omega\mu_0 \mathbf{H}, \tag{1}$$

$$\nabla \times \mathbf{H} = \hat{\boldsymbol{\sigma}}\mathbf{E}, \tag{2}$$

where a time factor $\exp(-i\omega t)$ is assumed. By virtue of the 2-D condition $\partial/\partial x = 0$, these equations, written for the individual components, reduce to

$$\frac{\partial E_z}{\partial y} - \frac{\partial E_y}{\partial z} = i\omega\mu_0 H_x, \tag{3}$$

$$\frac{\partial E_x}{\partial z} = i\omega\mu_0 H_y, \tag{4}$$

$$-\frac{\partial E_x}{\partial y} = i\omega\mu_0 H_z, \tag{5}$$

$$\frac{\partial H_z}{\partial y} - \frac{\partial H_y}{\partial z} = \sigma_{xx}E_x + \sigma_{xy}E_y + \sigma_{xz}E_z, \tag{6}$$

$$\frac{\partial H_x}{\partial z} = \sigma_{yx}E_x + \sigma_{yy}E_y + \sigma_{yz}E_z, \tag{7}$$

$$-\frac{\partial H_x}{\partial y} = \sigma_{zx}E_x + \sigma_{zy}E_y + \sigma_{zz}E_z. \tag{8}$$

We will suppose throughout this paper that the conductivity tensor within the earth's conductor,

$$\hat{\boldsymbol{\sigma}} = \begin{pmatrix} \sigma_{xx} & \sigma_{xy} & \sigma_{xz} \\ \sigma_{yx} & \sigma_{yy} & \sigma_{yz} \\ \sigma_{zx} & \sigma_{zy} & \sigma_{zz} \end{pmatrix},$$

is symmetric and positive-definite (or positive-semi-definite if the non-conductive air layer is considered). Then the conductivity tensor can be defined by its three principal values and by three rotation angles, analogous to Euler's elementary rotations known from classical mechanics. The conductivity tensor is constructed by successively applying three rotations to its diagonal, principal form—first, around the z-axis by the anisotropy strike α_S, then around the new x-axis by the anisotropy dip α_D, and finally around the latest z-axis by the slant angle α_L. In this way, any orientation of the principal axes of the conductivity tensor in space can be achieved.

To complete the mathematical formulation of the problem we must supply the boundary conditions for the field components, both on the inner and outer boundaries of the model. On inner boundaries, where blocks with different electrical properties make contact, the following conditions must hold: (i) continuity of the tangential component of the electric field $\mathbf{E}_\tau$; (ii) continuity of the normal component of the current density $j_n = \hat{\boldsymbol{\sigma}}\mathbf{E}\cdot\mathbf{n}$; and (iii) continuity of all the components of

the magnetic field **H**, as we assume the magnetic permeability to be equal to the vacuum value, $\mu = \mu_0 = 4\pi \times 10^{-7}$ H m^{-1}, everywhere within the model.

On the outer boundaries of the model, Dirichlet boundary conditions can be set, constructed from 1-D solutions for the corresponding layered media at the left- and right-hand sides of the model. In our version of the algorithm this is accomplished by applying a matrix propagation method to the vector composed of the horizontal components of the magnetotelluric field. This procedure can be considered as a slight modification of well-known techniques developed by Reddy & Rankin (1971) or Loewenthal & Landisman (1973). At the top and the bottom of the model the boundary conditions are constructed simply as linear interpolations of the respective 1-D values at the left- and right-hand margins of the model. If the layered structures on both the left-hand side and right-hand side of the model are the same, then the top boundary conditions are uniform E_x at the top of the air layer, placed on top of the model for the higher spatial harmonics in E_x to attenuate, and uniform H_x directly on the surface of the earth.

From eqs (3) to (8), the field components E_y, E_z, H_y, and H_z can be eliminated, which, after some algebra, yields a *coupled* pair of second-order partial differential equations for E_x and H_x:

$$\frac{\partial^2 E_x}{\partial y^2} + \frac{\partial^2 E_x}{\partial z^2} + i\omega\mu_0(\sigma_{xx} + A\sigma_{zx} + B\sigma_{xy})E_x + i\omega\mu_0 A\frac{\partial H_x}{\partial y} + i\omega\mu_0 B\frac{\partial H_x}{\partial z} = 0 \qquad (9)$$

for the E-mode, where

$$A = (\sigma_{xy}\sigma_{yz} - \sigma_{xz}\sigma_{yy})/D\,, \qquad B = (\sigma_{xz}\sigma_{yz} - \sigma_{xy}\sigma_{zz})/D\,,$$

$$D = \sigma_{yy}\sigma_{zz} - \sigma_{yz}^2\,,$$

and, for the H-mode, with the symmetry of the conductivity tensor employed,

$$\frac{\partial}{\partial y}\left(\frac{\sigma_{yy}}{D}\frac{\partial H_x}{\partial y}\right) + \frac{\partial}{\partial z}\left(\frac{\sigma_{zz}}{D}\frac{\partial H_x}{\partial z}\right) + \frac{\partial}{\partial y}\left(\frac{\sigma_{yz}}{D}\frac{\partial H_x}{\partial z}\right) + \frac{\partial}{\partial z}\left(\frac{\sigma_{yz}}{D}\frac{\partial H_x}{\partial y}\right) + i\omega\mu_0 H_x - \frac{\partial(BE_x)}{\partial y} + \frac{\partial(AE_x)}{\partial z} = 0\,. \qquad (10)$$

Of course, there is not a 'pure' E-mode or H-mode any more in generally anisotropic media. The coupling between the modes is expressed through the first-order terms in eqs (9) and (10). For these terms to vanish, the conductivity tensor must be of a degenerate form with $\sigma_{xz} = \sigma_{xy} = 0$, i.e. the coupling between the field modes dissolves if both the anisotropy strike and slant are zero, $\alpha_S = \alpha_L = 0$. Then, eqs (9) and (10) decouple into two separate 'pure' field modes. The conductivity tensor then reduces to

$$\hat{\boldsymbol{\sigma}} = \begin{pmatrix} \sigma_{xx} & \mathbf{0} \\ \mathbf{0}^{\mathrm{T}} & \hat{\boldsymbol{\sigma}}^{\mathrm{H}} \end{pmatrix},$$

where **0** is the zero-vector, and

$$\hat{\boldsymbol{\sigma}}^{\mathrm{H}} = \begin{pmatrix} \sigma_{yy} & \sigma_{yz} \\ \sigma_{yz} & \sigma_{zz} \end{pmatrix}$$

describes the dipping anisotropy in the H-polarization mode. Non-zero values of the non-diagonal elements of $\hat{\boldsymbol{\sigma}}^{\mathrm{H}}$ cause the mixed-derivative terms to appear in (10).

3 NUMERICAL APPROXIMATION

To approximate numerically the governing equations (9) and (10) we will use the finite-difference (FD) method in the traditional way it was used earlier to model 2-D isotropic structures (e.g. Haak 1972; Brewitt-Taylor & Weaver 1976; Červ & Praus 1978). First of all, the structure is projected onto a numerical grid and, within a finite grid region, subdivided into a system of electrically homogeneous, but in general anisotropic, rectangular grid cells. The grid is in general irregular and it should both fit the geometry of the model under study and meet general rules accepted for designing numerical grids in induction modelling studies for isotropic structures (e.g. Yudin 1982), respecting, however, the fact that, unlike scalar conductivities in isotropic structures, the tensorial conductivities are characterized by a range of values rather than by a single value.

Following Červ & Praus (1978), we use the integro-interpolation method to derive the FD equations for individual grid nodes. In this approach, eqs (9) and (10) are integrated across a rectangular integration cell, say

$$\left[y_j - \frac{1}{2}\Delta y_j,\, y_j + \frac{1}{2}\Delta y_{j+1}\right] \times \left[z_k - \frac{1}{2}\Delta z_k,\, z_k + \frac{1}{2}\Delta z_{k+1}\right] = [y_j^-, y_j^+] \times [z_k^-, z_k^+] = G_{jk}$$

if node (j, k) is considered (Fig. 1), and these integrals are then approximated around the respective grid point. Thus, the integral rather than the differential form of the basic field eqs (9) and (10) is used for the FD approximation. For more details on the mathematical background of the method see for example Červ & Praus (1978).

To avoid the explicit presentation of the whole integration process here, which is a straightforward, but quite tedious, procedure, we will illustrate the basic approximation steps by immediately referring to the equivalent integral form of Maxwell's equations, specified for the integration cell G_{jk} defined above. Eq. (9) represents another form of (6), with the y and z field components eliminated by making use of the other equations. The corresponding integral form of this equation, representing the x-projection of

$$\oint_{\Gamma(G_{jk})} \mathbf{H}\cdot d\mathbf{g} = \int_{G_{jk}} (\hat{\boldsymbol{\sigma}}\mathbf{E})\cdot d\mathbf{G}\,,$$

where $\Gamma(G_{jk})$ is the oriented boundary of the integration cell G_{jk}, $d\mathbf{g}$ is the element of the integration path along this boundary, and $d\mathbf{G} = dG\mathbf{e}_x$, with $\mathbf{e}_x$ denoting the unit vector in the x-direction and dG an areal element of G_{jk}, can be written as

$$\left(\widehat{\frac{\partial E_x}{\partial z}}\right)_{KL}\overline{KL} - \left(\widehat{\frac{\partial E_x}{\partial y}}\right)_{LN}\overline{LN} + \left(\widehat{\frac{\partial E_x}{\partial z}}\right)_{NM}\overline{NM} - \left(\widehat{\frac{\partial E_x}{\partial y}}\right)_{MK}\overline{MK} - i\omega\mu_0 S(G_{jk})\widehat{(j_x)}_{G_{jk}} = 0, \qquad (11)$$

where $\widehat{(v)}_\gamma$ is the mean value of the function $v(y, z)$ across γ (either a section of the boundary, or the integration cell), $\overline{P_1P_2}$ is the (oriented positive counter-clockwise when looking from the positive x-direction) distance between the

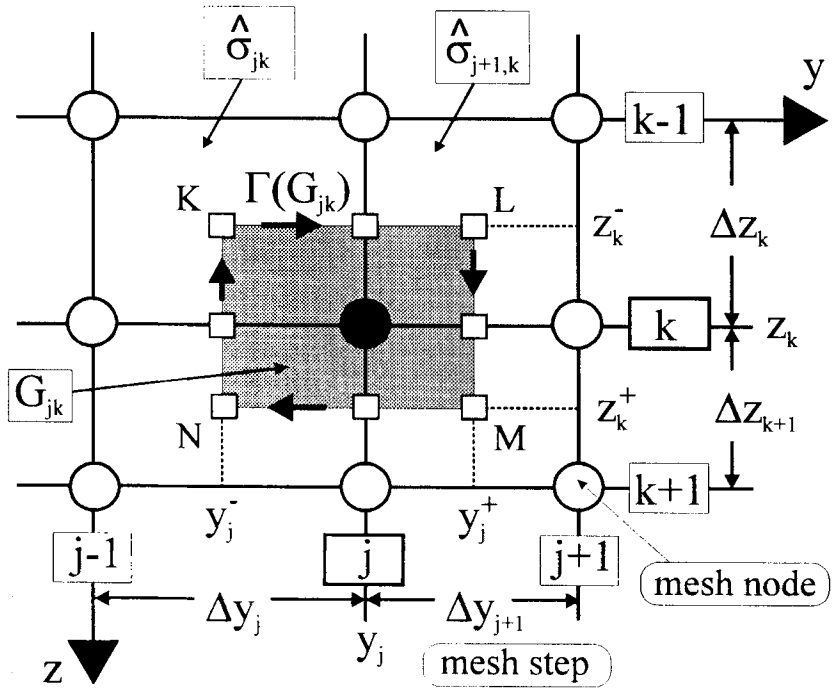

Figure 1. Section of the finite-difference grid around the node point (j, k), along with the geometrical parameters.

corresponding vertices of the integration cell, $S(G_{jk})$ the area of the integration cell, and $j_x = (\hat{\boldsymbol{\sigma}}\mathbf{E})_x = \sigma_{xx}E_x + \sigma_{xy}E_y + \sigma_{xz}E_z$ is the x-component of the current density.

Approximating the mean value of the derivative in, for example, the first term of eq. (11) by the appropriate difference of the nodal values, we obtain

$$\left(\widehat{\frac{\partial E_x}{\partial z}}\right)_{KL} \overline{KL} \approx \frac{\Delta y_j + \Delta y_{j+1}}{2\Delta z_k}\left[E_x(j, k) - E_x(j, k-1)\right],$$

where symbolic notation is introduced, for example $E_x(y_j, z_k) \equiv E_x(j, k)$. The other three terms can be approximated in the same way.

To approximate the last term on the left-hand side of (11), we first express the current density j_x in terms of E_x and H_x,

$$j_x = WE_x + A\frac{\partial H_x}{\partial y} + B\frac{\partial H_x}{\partial z},$$

where $W = \sigma_{xx} + A\sigma_{zx} + B\sigma_{xy}$, and then write

$$-i\omega\mu_0 S(G_{jk})\widehat{(j_x)}_{G_{jk}} \approx -i\omega\mu_0 \overline{W}_{jk}E_x(j, k) - i\omega\mu_0 \times \int_{y_j^-}^{y_j^+}\int_{z_k^-}^{z_k^+}\left(A\frac{\partial H_x}{\partial y} + B\frac{\partial H_x}{\partial z}\right)dydz, \quad (12)$$

where $\overline{W}_{jk}$ is the total conductance within the integration cell G_{jk},

$$\overline{W}_{jk} = \frac{1}{4}(\Delta y_j \Delta z_k W_{jk} + \Delta y_{j+1}\Delta z_k W_{j+1,k} + \Delta y_j \Delta z_{k+1} W_{j,k+1} + \Delta y_{j+1}\Delta z_{k+1} W_{j+1,k+1}).$$

The integral in (12) is computed directly by separating it into four integrals, each across one of the individual homogeneous subcells of the integration cell G_{jk}. So, for example, integrating the first integral term in (12) across the subcell $[y_j^-, y_j] \times [z_k^-, z_k]$ gives

$$-i\omega\mu_0 \int_{y_j^-}^{y_j}\int_{z_k^-}^{z_k} A\frac{\partial H_x}{\partial y}\,dydz = -i\omega\mu_0 A_{jk}\int_{z_k^-}^{z_k}\left[H_x(y_j, z) - H_x(y_j^-, z)\right]dz \approx -\frac{i\omega\mu_0}{4}\Delta z_k A_{jk}\left[H_x(j, k) - H_x(j-1, k)\right],$$

where the following approximations are used for z within the interval $[z_k^-, z_k]$:

$$H_x(y_j, z) \approx H_x(j, k),$$

$$H_x(y_j^-, z) \approx \frac{1}{2}\left[H_x(j, k) + H_x(j-1, k)\right]$$

(see Fig. 1).

Applying the approximation steps outlined above to all the terms of eq. (11) we arrive at an approximate difference equation for the 'E-mode' at the (j, k)th mesh node, which represents the FD approximation of eq. (9) and is in general of the form

$$\sum_{p=j-1}^{j+1}\sum_{q=k-1}^{k+1} C_{jk}^{EE}(p, q)E_x(p, q) + \sum_{p=j-1}^{j+1}\sum_{q=k-1}^{k+1} C_{jk}^{EH}(p, q)H_x(p, q) = 0, \quad (13)$$

with

$$C_{jk}^{EE}(p, q) = C_{jk}^{EH}(p, q) = 0$$

for

$$(p, q) \in \{(j-1, k-1), (j-1, k+1), (j+1, k-1), (j+1, k+1)\}.$$

The corresponding integral form of the 'H-mode', eq. (10), is given by the x-projection of eq. (3) integrated across the cell G_{jk},

$$\oint_{\Gamma(G_{jk})} \mathbf{E}\cdot d\mathbf{g} = i\omega\mu_0 \int_{G_{jk}} \mathbf{H}\cdot d\mathbf{G},$$

which yields

$$\widehat{(E_y)}_{KL}\overline{KL} + \widehat{(E_z)}_{LN}\overline{LN} + \widehat{(E_y)}_{NM}\overline{NM} + \widehat{(E_z)}_{MK}\overline{MK} - i\omega\mu_0 S(G_{jk})\widehat{(H_x)}_{G_{jk}} = 0. \quad (14)$$

Using (7) and (8), we can express E_y and E_z by means of the 'basic' components E_x, H_x:

$$E_y = \frac{\sigma_{zz}}{D}\frac{\partial H_x}{\partial z} + \frac{\sigma_{yz}}{D}\frac{\partial H_x}{\partial y} + \frac{B}{D}E_x,$$

$$E_z = -\frac{\sigma_{yy}}{D}\frac{\partial H_x}{\partial z} - \frac{\sigma_{yz}}{D}\frac{\partial H_x}{\partial z} + \frac{A}{D}E_x. \quad (15)$$

Thus, considering, for example, the first term in (14), we can approximate it separately for its three individual sub-terms. The first one represents a generalized form already encountered in the traditional isotropic H-mode case, and is easily approximated by substituting the difference of nodal values for the vertical derivative:

$$\widehat{\left(\frac{\sigma_{zz}}{D}\frac{\partial H_x}{\partial z}\right)}_{KL}\overline{KL} \approx \frac{1}{2\Delta z_k}\left[\Delta y_j\left(\frac{\sigma_{zz}}{D}\right)_{jk} + \Delta y_{j+1}\left(\frac{\sigma_{zz}}{D}\right)_{j+1,k}\right] \times [H_x(j,k) - H_x(j,k-1)].$$

The second sub-term arises due to dipping anisotropy ($\sigma_{yz} \neq 0$) and can be written

$$\begin{aligned}\widehat{\left(\frac{\sigma_{yz}}{D}\frac{\partial H_x}{\partial y}\right)}_{KL}\overline{KL} &= \left(\frac{\sigma_{yz}}{D}\right)_{jk}[H_x(y_j, z_k^-) - H_x(y_j^-, z_k^-)] \\ &\quad + \left(\frac{\sigma_{yz}}{D}\right)_{j+1,k}[H_x(y_j^+, z_k^-) - H_x(y_j, z_k^-)] \\ &\approx \frac{1}{4}\left(\frac{\sigma_{yz}}{D}\right)_{jk}[H_x(j,k) + H_x(j,k-1) \\ &\quad - H_x(j-1,k) - H_x(j-1,k-1)] \\ &\quad - \frac{1}{4}\left(\frac{\sigma_{yz}}{D}\right)_{j+1,k}[H_x(j,k) + H_x(j,k-1) \\ &\quad - H_x(j+1,k) - H_x(j+1,k-1)],\end{aligned}$$

where the values of H_x on the sides and at the apices of the integration cell G_{jk} are again approximated by averages of the adjacent nodal values (see Fig. 1), for example

$$H_x(y_j, z_k^-) \approx \frac{1}{2}[H_x(j,k) + H_x(j,k-1)],$$

$$H_x(y_j^-, z_k^-) \approx \frac{1}{4}[H_x(j,k) + H_x(j-1,k) + H_x(j-1,k-1) + H_x(j,k-1)].$$

The third sub-term contains the electrical component E_x and represents the contribution of the inter-mode coupling due to the anisotropy. It can be approximately written as

$$\widehat{\left(\frac{B}{D}E_x\right)}_{KL}\overline{KL} \approx \frac{1}{4}\left[\Delta y_j\left(\frac{B}{D}\right)_{jk} + \Delta y_{j+1}\left(\frac{B}{D}\right)_{j+1,k}\right] \times [E_x(j,k) + E_x(j,k-1)].$$

Applying the approximation steps outlined here to all the terms in (14), and approximating the last term by

$$-i\omega\mu_0 S(G_{jk})\widehat{(H_x)}_{G_{jk}} \approx -\frac{i\omega\mu_0}{4}(\Delta y_j + \Delta y_{j+1}) \times (\Delta z_k + \Delta z_{k+1})H_x(j,k),$$

we finally arrive at the linear difference equation for the H-mode at the (j,k)th mesh node:

$$\sum_{p=j-1}^{j+1}\sum_{q=k-1}^{k+1} C_{jk}^{HE}(p,q)E_x(p,q) + \sum_{p=j-1}^{j+1}\sum_{q=k-1}^{k+1} C_{jk}^{HH}(p,q)H_x(p,q) = 0. \quad (16)$$

As opposed to the analogous equation (13) for the E-mode, in eq. (16), only $C_{jk}^{HE}(p,q) = 0$ for

$$(p,q) \in \{(j-1,k-1), (j+1,k-1), (j-1,k+1), (j+1,k+1)\}.$$

The corresponding 'magnetic' coefficients $C_{jk}^{HH}(p,q)$ do not in general vanish at these nodes, and do express the effect of dipping anisotropy, i.e. they are present even in the case of dipping anisotropy in the pure H-mode when no inter-mode coupling takes place.

Thus, to summarize, for an arbitrary grid point (j,k) the FD approximation results in a pair of linear algebraic equations, (13) and (16), which relate the components E_x and H_x at the central node (j,k) to their eight nearest neighbours in the grid. If a grid point involved in eqs (13) and (16) falls on the outer boundary of the grid region, then the field values at this node are replaced by the appropriate boundary conditions, and the corresponding terms are transferred to the right-hand sides of eqs (13) and (16).

In the Appendix, all the coefficients $C_{jk}^{\alpha\beta}(p,q)$, $\alpha, \beta \in \{E, H\}$, $p = j-1, j, j+1$, $q = k-1, k, k+1$, are given explicitly. From these FD scheme patterns, it can be seen that the matrix of coefficients $C_{jk}^{\alpha\beta}(p,q)$ is never fully occupied, i.e. we need not deal with a 9-point (i.e. 18-value) scheme in any case. For the E-mode, we have a 5-point (10-value) scheme only. For the H-mode, a complete 9-point scheme must be considered; it contains, however, 14 non-zero coefficients only. These are the maximum numbers of coefficients, with full anisotropy, considered. The number of non-zero coefficients will decrease as the anisotropy within the grid cells involved degenerates.

The FD scheme simplifies particularly within the insulating air-layer. By virtue of eqs (7) and (8), $\partial H_x/\partial z = 0$ and $\partial H_x/\partial y = 0$ in the air, i.e. H_x must be constant everywhere in the air, and eq. (10) need not be approximated at all. Eq. (9) reduces to the Laplace equation. Hence, within the air layer only the E-mode equation is FD approximated, which yields a 5-point FD scheme with only five coefficients C_{jk}^{EE}.

4 SOLUTION OF THE FD EQUATIONS

Having the governing field equations (9) and (10) FD approximated in all grid nodes, the linear algebraic equations (13), (16) must be properly arranged into a system for further treatment. This may seem a rather intricate task, since two sets of variables are involved, E_x and H_x. Moreover, these variables are not sought on identical sets of grid nodes—while the E-mode equation is approximated throughout the grid, the H-mode equation is to be solved within the conducting earth only.

Two possibilities for arranging the variables into an array seem obvious (Fig. 2). For both, we will order the variables throughout the grid in a column-by-column manner, but a row-by-row alternative is possible as well. In the first variant, (i), at first all electric variables are ordered throughout the grid, from the top to the bottom within each column, and afterwards a block of magnetic variables inside the earth, ordered in the same way, is joined to the electric subarray (Fig. 2, left). In the second variant, (ii), within a column, electric variables are ordered in succession from the top of the column to the earth's surface, and then, inside the earth, electric and magnetic components are stacked up alternately until the bottom of the column is reached. Then the next column is taken and processed in the same way (Fig. 2, right), until the whole mesh is deployed.

Each of these arrangements of the variables leads to a specific form of the matrix of the system of linear algebraic equations for the approximate field values. Arrangement (i) gives a four-block matrix which contains the principal mode coefficients in the diagonal blocks, and the coupling coefficients in the anti-diagonal blocks (Fig. 2, left). For isotropic structure, the two field modes, E and H, obviously separate into two independent matrices.

Arrangement (ii) mixes the principal mode coefficients and those arising due to inter-mode coupling together within each row of the matrix, but leads to a more compact, band-limited matrix (Fig. 2, right). Although we have not attempted an exact proof, in our opinion this arrangement (or the corresponding row-to-row analogy of it, depending on the number of grid points in the horizontal and vertical directions) yields a matrix with the narrowest band possible for the particular mesh division. It can easily be shown that, after multiplying all the H-mode equations by a constant factor $i\omega\mu_0$, the matrix is symmetric [the same applies, naturally, to matrix (i)]. Here, we prefer arrangement (ii), as it allows Gaussian elimination, in a special modification for symmetric, band-limited matrices, to be used to solve the FD linear algebraic system. To store the

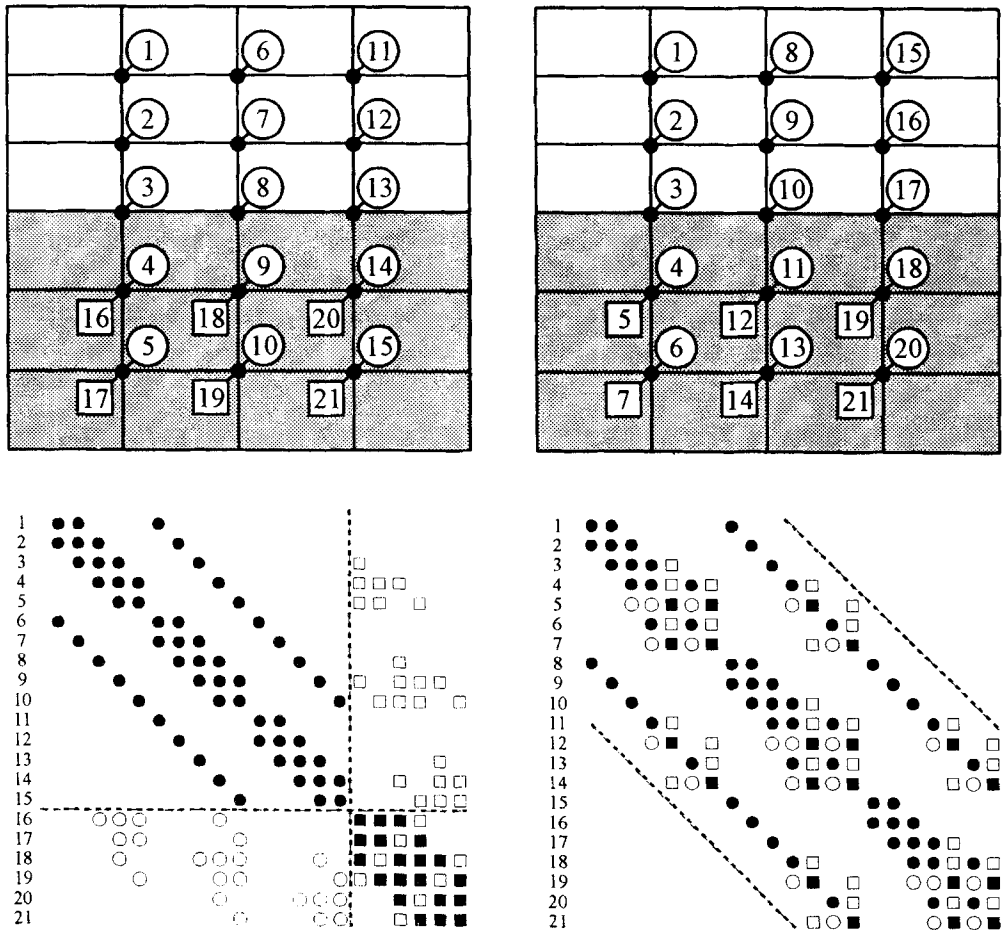

Figure 2. Two variants of ordering the variables throughout the grid, along with a symbolic form of the resulting matrix of the system of FD equations. Circles are for electric components, squares for magnetic components, empty symbols in the matrix patterns are for coefficients which arise only due to anisotropy.

upper half-band of the matrix, as required by the modified algorithm of Gaussian elimination, N_{STOR} complex numbers need to be placed in memory,

$$N_{STOR} = \underbrace{(N-1)(2M_E + M_A - 2)}_{\text{number of equations}} \underbrace{(2M_E + M_A + 1)}_{\text{band-width}},$$

where N is the number of horizontal grid steps, and M_E, M_A are the numbers of vertical grid steps within the conducting earth and in the air layer, respectively. This is usually by far the most memory-consuming part of the modelling algorithm.

As regards the computation time, Gaussian elimination is also the most time-consuming procedure of the algorithm. The time required increases rapidly for large grids, in particular with increasing number of vertical grid points (in the case of column-by-column arrangement of the nodes). On a PC 486/66 MHz, with 32-bit Lahey FORTRAN used to compile the program, typical times required to compute the solution for two independent polarizations of the field and to evaluate the standard magnetotelluric functions on the surface for one period were 21 s for the mesh parameters $(N, M_E, M_A) = (40, 20, 10)$, 44 s for (40, 25, 15), 95 s with (40, 35, 15), and 195 s for (80, 35, 15).

5 MAGNETOTELLURIC FUNCTIONS ON THE EARTH'S SURFACE

Solving the system of linear FD equations (13) and (16) provides us with approximate values of the field components E_x and H_x at all grid points. For practical purposes, all components of the magnetotelluric field must be evaluated at the earth–air interface. From these, various magnetotelluric functions and parameters can be computed as practice-oriented modelling outputs.

With knowledge of E_x and H_x throughout the grid, values of the 'secondary' field components E_y, E_z, H_y, and H_z can be evaluated at any grid point using eqs (4), (5), and (15):

$$E_y = \frac{\sigma_{yz}}{D}\frac{\partial H_x}{\partial y} + \frac{\sigma_{zz}}{D}\frac{\partial H_x}{\partial z} + AE_x, \qquad H_y = \frac{1}{i\omega\mu_0}\frac{\partial E_x}{\partial z},$$

$$E_z = -\frac{\sigma_{yy}}{D}\frac{\partial H_x}{\partial y} - \frac{\sigma_{yz}}{D}\frac{\partial H_x}{\partial z} + BE_x, \qquad H_z = -\frac{1}{i\omega\mu_0}\frac{\partial E_x}{\partial y}.$$

On the surface, $\partial H_x/\partial y = 0$, as no vertical current can flow through the earth–air interface, but, in contrast to the isotropic case, E_z does not in general vanish immediately below the earth's surface. The field components on the surface are computed by approximating numerically the derivatives $\partial E_x/\partial y$, $\partial E_x/\partial z$, and $\partial H_x/\partial z$ in the above formulae.

The magnetotelluric and geomagnetic transfer functions on the earth's surface (impedances, admittances, components of the induction vectors, etc.) are evaluated using the field components computed for two independent polarizations of the primary electromagnetic wave. Anisotropy within a 2-D structure leads in general to a full and non-diagonizable impedance tensor, thus imitating locally a 3-D underground. Other magnetotelluric parameters, such as Swift's principal direction, skew, ellipticity, etc., can now be computed easily.

6 NUMERICAL TESTS

There are only a few opportunities to check the results of the modelling algorithm presented with other independent computations. As well as for some trivial checks, such as the identity of the magnetotelluric functions when different polarizations of the primary wave are used, we carried out the following tests.

(1) The results of the present algorithm for an isotropic structure are identical with those obtained independently by a 2-D 'isotropic' modelling program by Červ & Praus (1978) for the same model.

(2) The results for a 1-D anisotropic layered structure, approximated as a 2-D model, are practically identical with those obtained independently by a 1-D algorithm based on the matrix propagation of the electromagnetic fields through the layers. The deviations do not exceed 2 per cent in modulus and 1° in phase (Fig. 3). The systematic increase of the error towards the bottom of the model is due to a rapid mesh coarsening at greater depths. The jumps observed in the plots are attributed to layer boundaries with large contrasts of the electrical conductivities. These effects can be reduced by refining the FD mesh, although, of course, at the cost of increased demands on computer resources.

(3) Reddy & Rankin (1975) studied a 2-D horizontally anisotropic dyke model in detail. In Fig. 4, a comparison of our results with those taken from their paper is shown for a set of magnetotelluric functions—apparent resistivities and impedance phases. For this model the results are almost identical: very small differences are observed only near the dyke contacts, where the difference between the approximations is likely to play some role.

7 NUMERICAL EXAMPLES—NON-TRIVIAL PHENOMENA

In what follows, we will demonstrate the developed algorithm by showing a few simple models which illustrate the effect of large electrical anisotropy upon the magnetotelluric functions and induction arrows. We will particularly concentrate on phenomena which seem to be not quite trivial consequences of the electrical anisotropy and which might be of value for the interpretation of practical data in situations when significant anisotropy is suspected to affect the magnetotelluric field observed. To demonstrate the effects analysed as clearly as possible, we have chosen rather exaggerated anisotropies and geometrical dimensions of the relevant structures in the models presented in this section.

Example 1: distortions of the induction arrows by anisotropic structures

In the first example, we study the influence of anisotropic structures on the induction arrows. We have chosen these models since absolutely nothing could have been said earlier about induction arrows in anisotropic structures with solely 1-D modelling algorithms available.

The model in Fig. 5 consists of a two-layer earth with an anisotropic half-layer inserted in the first layer. The principal resistivities of the anisotropic inhomogeneity are $\rho_{\xi\xi}/\rho_{\eta\eta}/\rho_{zz}$ = 3/100/3, in Ω m, and the anisotropy strike, α_S, is 30° with respect to the structural strike of the model. ξ and η are the $\hat{\boldsymbol{\sigma}}$-principal horizontal coordinates resulting from the rotation of the original x, y-coordinate system by α_S around the z-axis.

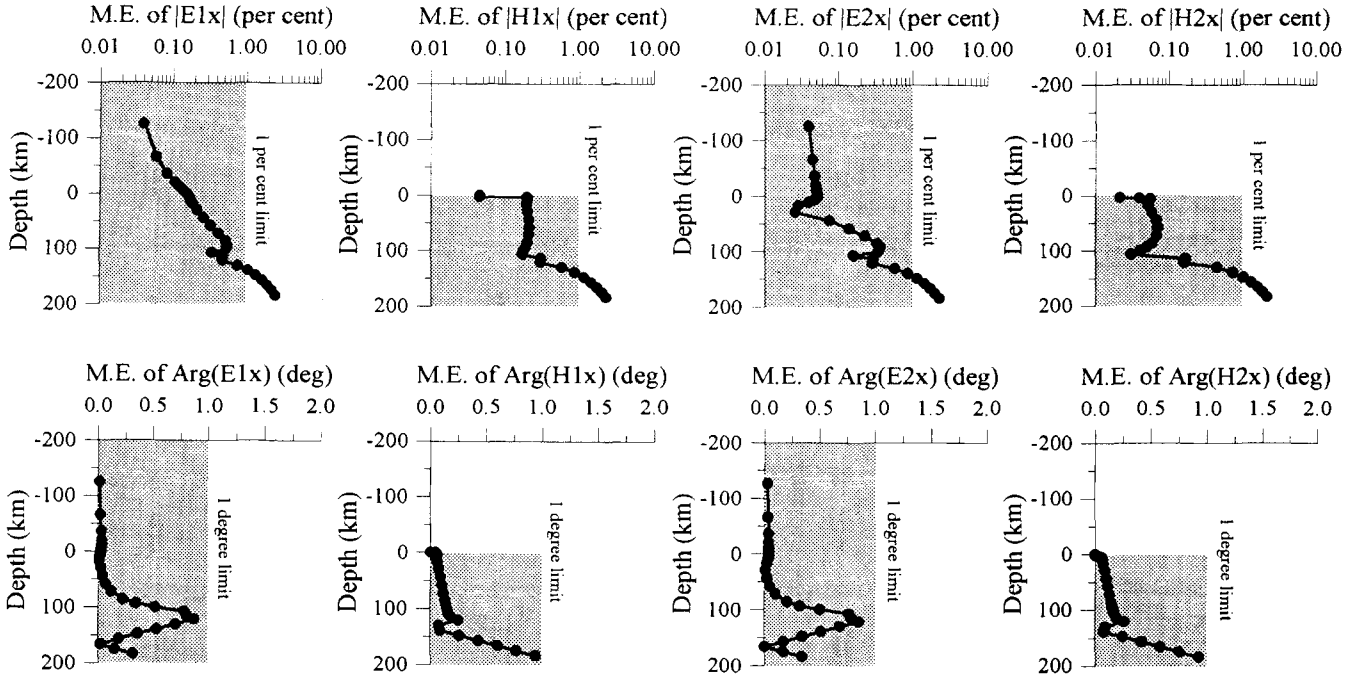

Figure 3. Comparison of the matrix propagation solution and that obtained by the present 2-D finite-difference algorithm for a 1-D anisotropic layered model with the following parameters: $h_1 = 0.5$ km, $\rho_1 = 100\ \Omega$ m, $h_2 = 1$ km, $\rho_2 = 3000\ \Omega$ m, $h_3 = 3$ km, $\rho_{3,\xi\xi}/\rho_{3,\eta\eta}/\rho_{3,zz} = 10/300/10\ \Omega$ m, anisotropy strike $\alpha_{S3} = 30°$, $h_5 = 101.5$ km, $\rho_5 = 1000\ \Omega$ m, $\rho_6 = 30\ \Omega$ m. ξ and η are the $\hat{\boldsymbol{\sigma}}$-principal horizontal coordinates resulting from the rotation of the original x, y-coordinate system by α_S around the z-axis. The period of the field is 100 s. The maximum error (M.E.) of the 2-D FD solution with respect to the 1-D analytic solution along each horizontal mesh line is displayed for modules and arguments of the components of the electromagnetic field for two perpendicular polarizations of the primary magnetic variations.

In the upper part of Fig. 5, the top view of the induction arrows and polar impedance diagrams for Z_{xx} and Z_{xy} is shown for selected points along the model's surface and for a series of periods from 10 to 3000 s. Under the influence of the anisotropic half-layer, the real induction arrows behave in a way qualitatively expected—they are deflected so as to preserve their perpendicular direction with respect to the predominant induced currents. Similar effect can be observed for the polar impedance diagrams Z_{xy} as well—their minimum axes indicate the direction of preferred conductivity, i.e. the anisotropy strike in this case. Immediately above the contact, the polar diagrams Z_{xy} change their orientation which reflects the remote influence of the discontinuity of E_y at the deep conductivity jump.

A different pattern, however, is observed if two isotropic domains make contact and the effect of an additional anisotropic layer is superimposed over that excited by the lateral inhomogeneity. The model in Fig. 6 is a modified version of the preceding model—the conductive half-layer is made isotropic, resistivity 3 Ω m, and is overlaid with an additional anisotropic layer, with principal resistivities $\rho_{\xi\xi}/\rho_{\eta\eta}/\rho_{zz} = 30/1000/30\ \Omega$ m and an anisotropy strike $\alpha_S = 30°$. In this case, the real induction arrows are oriented *in the direction of preferred conductivity of the anisotropic layer*, and not perpendicularly to it as one would expect. We explain this phenomenon by the effect of compensation currents within the conducting half-layer, which try to cancel out the vertical magnetic field excited by the j_x currents arising due to a deflection of perpendicular currents (j_y) in the anisotropic layer.

In Fig. 7, smoothed real current densities $\mathcal{R}e[j_x(y, z)]$ and $\mathcal{R}e[j_y(y, z)]$ are displayed in the vicinity of the deep contact for two polarizations of the primary magnetic field—polarization 1 with $\mathbf{H}_0 = (H_{0x}, H_{0y}, H_{0z}) = (0, 1, 0)$ (i.e. E-polarization in the isotropic case), and polarization 2 with $\mathbf{H}_0 = (-1, 0, 0)$ (H-polarization in the isotropic case). The period of the field is 30 s. In the case of polarization 1, the current distribution for j_x does not principally differ from that observed in the isotropic case. The strike-parallel currents are mostly concentrated within the good conductor and also partly within the less conductive anisotropic layer. The current deflection due to the anisotropy takes place solely within the anisotropic layer; perpendicular currents j_y are practically negligible everywhere outside this layer.

For polarization 2, the currents perpendicular to the structural strike again behave analogously to the isotropic case—they prefer flowing in the well-conducting half-layer, and, after they encounter the contact with the poor conductor, they escape into the less resistive anisotropic layer. Here, due to a deflection caused by the anisotropy, quite large positive parallel currents j_x come into existence which, in turn, induce secondary, *negative* Foucault currents in the underlying half-layer. From Fig. 7 it can be seen that, as to the magnitude, these compensating currents are comparable with the parallel currents generated in polarization 1 by the external magnetic field of the same amplitude. The vertical magnetic field of these negative currents, correlated now with the parallel magnetic component H_x, explains the rather large deflection of the real induction arrows towards the direction of preferred conductivity of the anisotropic layer.

An effect quite similar to that described above for an anisotropic cover is observed if the anisotropic layer is situated

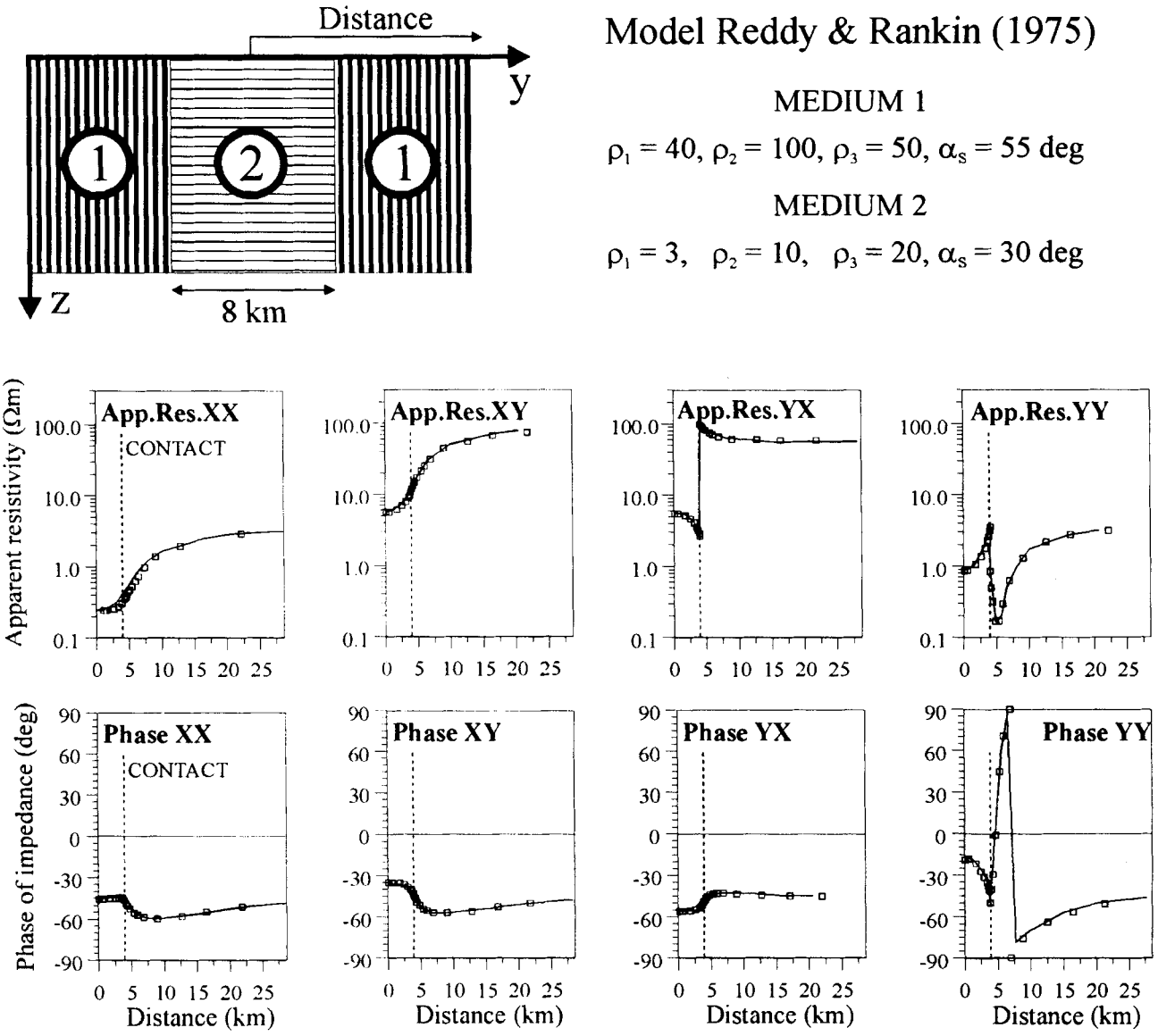

Figure 4. Comparison of apparent resistivities (top row of plots) and phases (bottom row of plots) for the horizontally anisotropic dyke model of Reddy & Rankin (1975). The results are displayed along a 25 km long section starting from the centre of the model and extending to the right. The dashed line at 4 km indicates the position of the contact. Solid line—modelling results by Reddy & Rankin (1975); squares—results obtained by the present FD algorithm.

below the lateral contact (Fig. 8): only the frequency range of the maximum influence of the anisotropy is shifted, owing to the greater depth of the layer, towards longer periods.

Example 2: vertical stack of anisotropic bodies with different anisotropy strikes

Another non-trivial effect is connected with the magnetotelluric phases at the contact of two generally anisotropic blocks. In isotropic models, when crossing an outcropping contact of two blocks with different conductivities, the apparent resistivities related to the telluric component perpendicular to the contact suffer a jump, but the corresponding phases pass the contact continuously. This is a general consequence of the continuity of the normal component of the current density at the contact, and in 2-D models it refers to the H-polarization field mode. Here, $j_n = j_y = \sigma E_y = \partial H_x/\partial z$, and, due to the continuity of H_x, E_y suffers a jump by the *real* factor $\sigma(y_c+, 0+)/\sigma(y_c-, 0+)$ at a contact located at $y = y_c$. This discontinuity affects the modulus of E_y, but evidently not its phase.

In an anisotropic medium the current density is in general given by a linear combination of all three components of the telluric field, and the phase of the telluric component perpendicular to a conductivity contact is no longer continuous at the contact. For certain configurations of the anisotropic domains, serious distortions of both the apparent resistivities and impedance phases can occur above outcropping anisotropic blocks.

By experimenting, we found such a highly anomalous distortion to take place for a model consisting of an outcropping anisotropic block underlain by an anisotropic layer with a different anisotropy strike (Fig. 9). If the outcrop is narrow enough and the two anisotropy strikes involved are near to

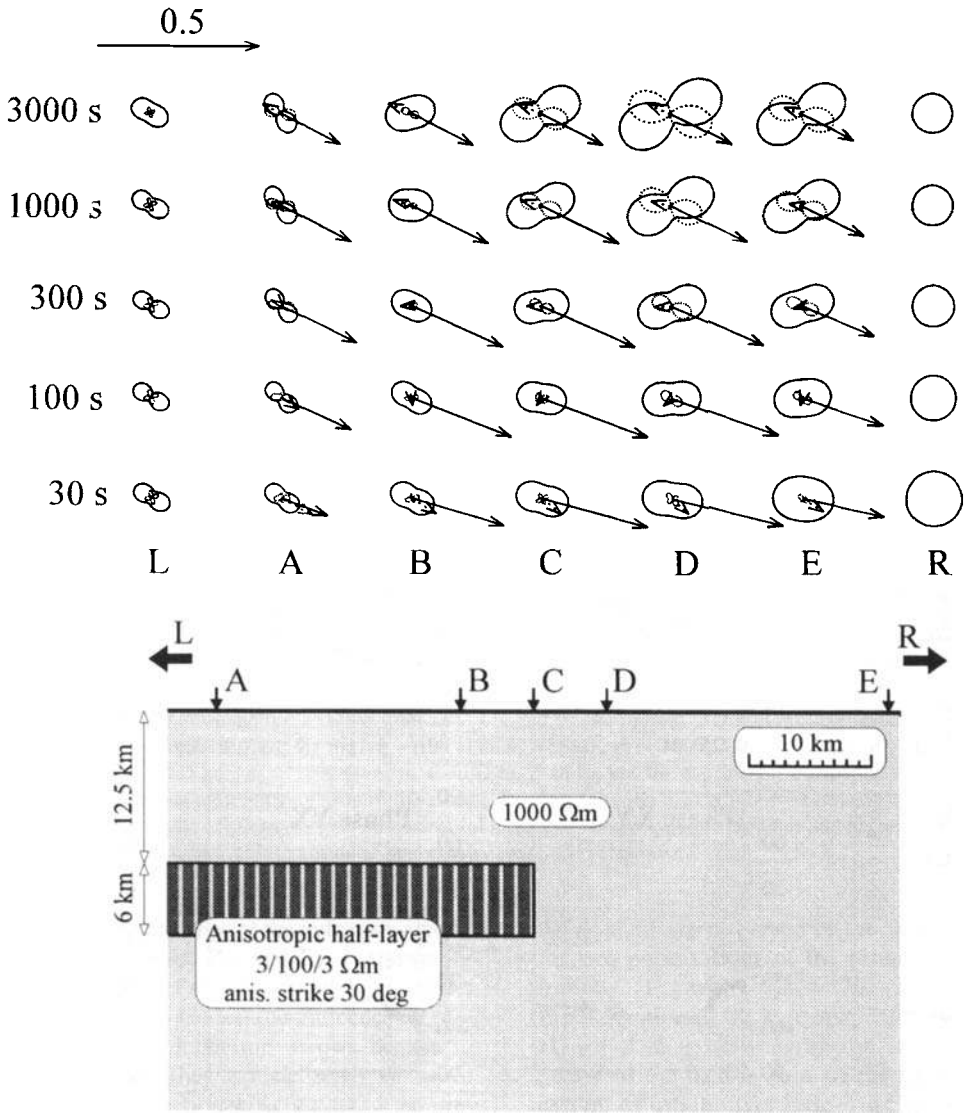

Figure 5. Top view of the real (full arrows) and imaginary (dashed arrows) induction arrows and polar impedance diagrams for a two-layer earth with an anisotropic half-layer inserted in the first layer. The conductivity tensor of the anisotropic layer is given by the principal resistivities $\rho_{\xi\xi}/\rho_{\eta\eta}/\rho_{zz} = 3/100/3\ \Omega$ m, and the anisotropy strike $\alpha_S = 30°$ towards R. All resistivities are in Ω m. The polar impedance diagrams are normalized in such a way that the principal axis of the main diagram at point L ($y_L = -\infty$ km) is the same for all periods.

perpendicular, the yx-phase jump does not recover across the whole anomalous block, and this phase totally leaves its 'natural' quadrant along the outcrop. In Fig. 10 we demonstrate this phenomenon by surface plots showing both the yx-apparent resistivity and phase near the contact as a function of the anisotropy strike of the base layer $\alpha_{S2} \in (30°, 210°)$, α_{S1} being 30°. The plot is constructed for a period of 30 s.

The figure shows that, in this particular situation, for anisotropy strikes that do not differ by more than about 45°, the yx-phase jump is generally very small, a few degrees at the most. For a greater divergence of the strikes, the yx-phase decreases rapidly above the anisotropic outcrop, the difference between the phases above the anomaly and those above the isotropic medium reaching as much as 180° directly at the contact, and more than 90° at the centre of the outcrop. Physically this means that, within some near-surface portion of the anisotropic outcropping block, the collinearity of the strike-perpendicular currents and telluric fields is impaired, or more specifically, the telluric field perpendicular to the structural strike is locally reversed with respect to the electric current. We tried to visualize this anomalous situation in Fig. 11 by comparing the projections, onto the vertical plane, of the current densities $\mathscr{Re}\ \mathbf{j}(y, z)$ and electric fields $\mathscr{Re}\ \mathbf{E}(y, z)$ within the anisotropic block. The figure clearly shows a zone where the electric intensity and current density are anti-parallel along the entire internal boundary of the block. The generating magnetic field is $\mathbf{H}_0 = (-1, 0, 0)$ (polarization 2) for this model, and the period of the field is 30 s. It must be emphasized, however, that the phenomenon described here refers to the (y, z)-projection of the electric intensities and current densities only. As a whole, due to the positive-definiteness of the conductivity tensor within the earth, the currents and electrical intensities can never be anti-parallel, although their directional difference can be quite large (as much as 60° in the present example).

The effect described above diminishes rapidly with

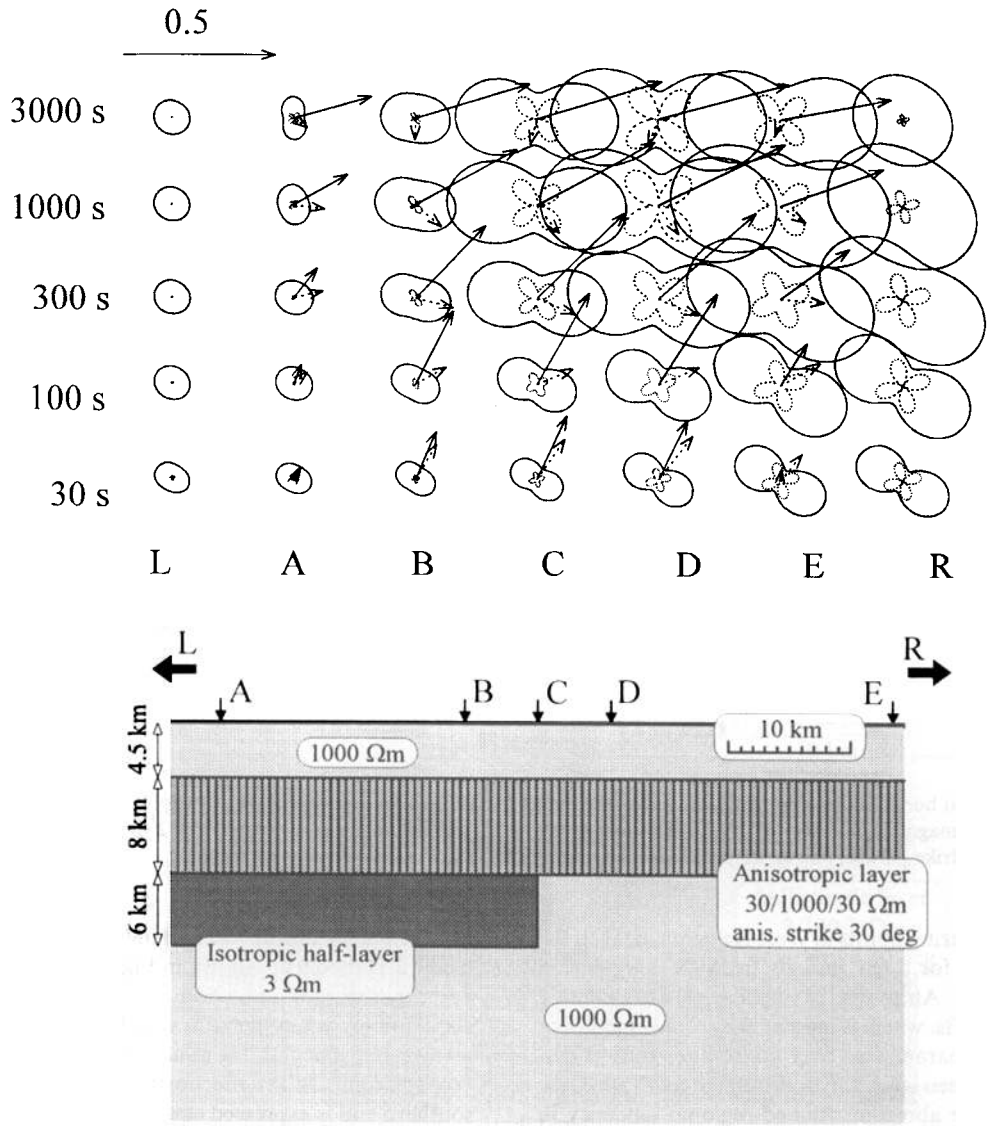

Figure 6. Top view of the real (full arrows) and imaginary (dashed arrows) induction arrows and polar impedance diagrams for a model with a lateral conductivity contact overlaid with an anisotropic layer. The conductivity tensor of the anisotropic layer is given by the principal resistivities $\rho_{\xi\xi}/\rho_{\eta\eta}/\rho_{zz} = 30/1000/30\ \Omega$ m and the anisotropy strike of 30° towards R. All resistivities are in Ω m. The normalization of the polar impedance diagrams is the same as in Fig. 5.

increasing width of the anisotropic block. For broader blocks, the anomalous behaviour of the *yx*-phase is restricted solely to very narrow intervals immediately around the contacts, and the phase recovers quickly outside those narrow contact zones.

The anomalous behaviour of the *yx*-phase is not necessarily connected with outcropping anisotropic dykes. The effect of the *yx*-phase leaving its 'natural' interval (90°, 180°) can be observed even in the case where the top of the anisotropic block is separated by some distance from the surface. The effect decreases, however, very rapidly with increasing depth of the structure. Of course, in the case of a submerged stack of anisotropic bodies, no phase jump is observed in the surface data.

Example 3: inconsistency of magnetotelluric principal directions and induction arrows in practical data from West Bohemia (Czech Republic)

We consider the results of the simple modellings presented above to be quite interesting with regard to the induction studies carried out in the regional vicinity of the deep drilling experiment KTB in Oberpfalz (Germany). A discrepancy often discussed when considering the induction data from this area consists of a regionally observed directional difference between the induction arrows and principal impedances—while the impedances display rather large anisotropy with minor axes of the impedance diagrams directed predominantly towards NW to NNW, the real induction arrows are almost uniformly directed towards the south, at least for longer periods over 10 s. This means that, according to the induction arrows, the regional structure strikes E–W and becomes gradually more resistive towards the south, as indicated by the decreasing moduli of the arrows. Magnetotelluric impedances indicate that the preferred conductivity of more local structures is oriented NW–SE. This directional pattern cannot be explained by a single 2-D model.

In Fig. 12(c), both the impedances and real induction arrows

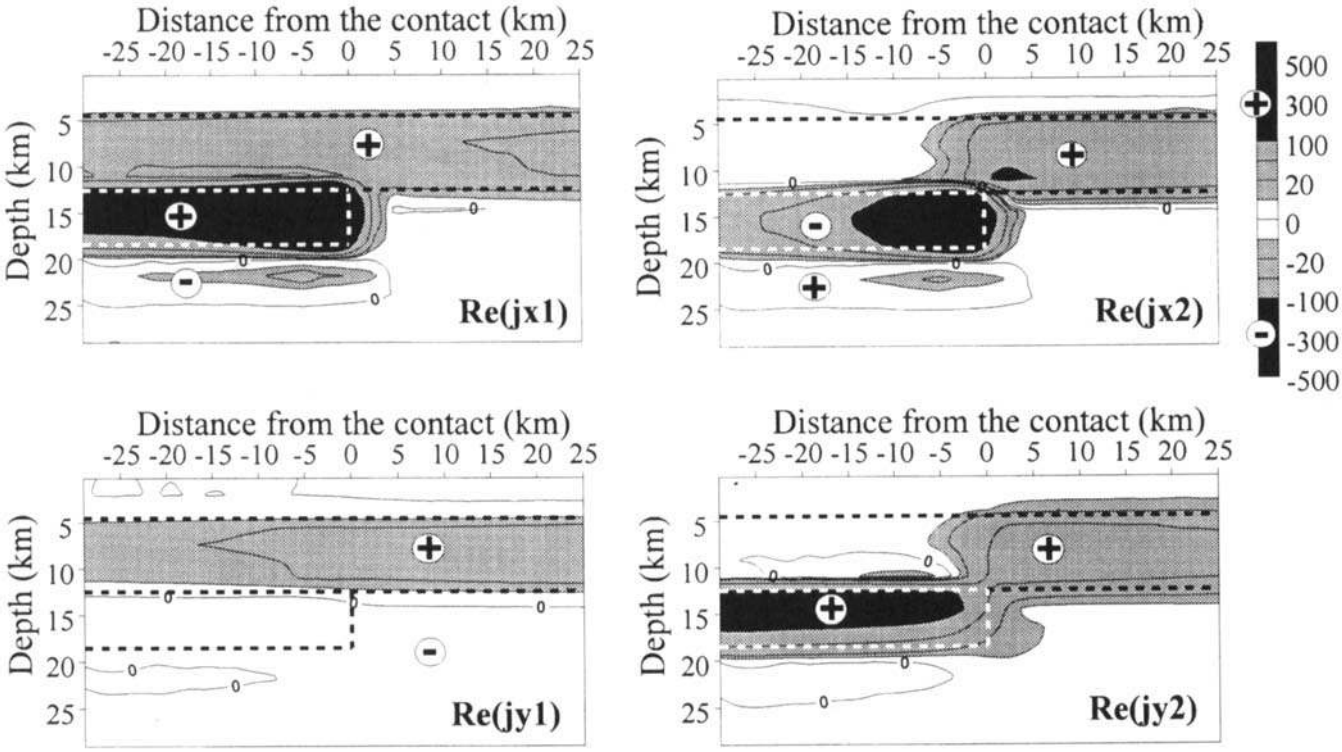

Figure 7. Smoothed real horizontal current densities within the model from Fig. 6 for a period of 30 s. The plots in the left-hand column are for polarization 1 (primary magnetic field $H_{0x} = 0$, $H_{0y} = 1$); those in the right-hand column are for polarization 2 (primary magnetic field $H_{0x} = -1$, $H_{0y} = 0$). *jx*, *jy* are the strike-parallel and strike-perpendicular components of the current density, respectively.

from a series of measuring points in West Bohemia, near to the KTB site, are shown for a few periods from the long-period magnetotelluric range. Although the impedances are evidently distorted by static shifts, which is indicated by rapid changes of the magnetotelluric parameters over short inter-station distances and has also been shown by a distortion analysis (Červ *et al.* 1993, 1994), the above-mentioned regional tendency in the mutual orientation of the impedances and real induction arrows can be clearly recognized in the data.

Eisel (1994) interpreted the large anisotropy, typical of his broad-band AMT/MT data from the immediate vicinity of the KTB drilling site, as an effect of the dyke macro-anisotropy. In his model of the Erbendorf–Vohenstrauss zone (ZEV), the principal feature is a highly anisotropic block situated in the upper-to-middle crust immediately beneath the ZEV. Towards the NE, this block seems to submerge to greater depths. The huge anisotropy of the block, with $\lambda = \rho_{max}/\rho_{min}$ exceeding 10^2, is considered to be caused by NW–SE striking, steeply dipping cataclastic zones filled with fluids, graphite and other conductive minerals. These zones are actually observed on the borehole lithology, and in the broader vicinity of the drilling site are detected by large anomalies of the spontaneous polarization.

One of the hypothetical interpretations of the magnetotelluric data from West Bohemia was based on Eisel's results (Červ *et al.* 1994) and represented a speculative extrapolation of his ZEV model further to the east, with the highly anisotropic block located in the crust and extending over a depth range from 4 to 10 km (Fig. 12b). The regional E–W structure was modelled by a single conductive half-layer in the middle crust, cut off before the northern end of the profile. The resulting impedances and real induction arrows for this anisotropic 2-D model are shown in Figure 12(d). The model data fit the experimental induction arrows satisfactorily, including some minor, yet systematic variations in the azimuths of the arrows. In particular, the minor deflection of the real induction arrows from east at the north of the profile to west at its southern end is expressed clearly by the model arrows.

As regards the magnetotelluric data, the minor axes of the impedance diagrams are systematically deflected towards the NW all along the profile and for all the period range considered. The anisotropy of the principal apparent resistivities exceeds the value of 60 for practically all sites. Of course, the rapid local variations of the experimental magnetotelluric data, caused most probably by the local static distortions, can hardly be rendered properly by a simple, schematic model like this. Nevertheless, without penetrating further into the details of physical or geological conditions and consequences of the problem, the numerical experiment has proved that, within the class of 2-D anisotropic models, the seemingly inconsistent relation between the impedances and induction arrows can be resolved.

8 CONCLUSION

In the present paper we have tried to describe a complete and general algorithm for the 2-D modelling in generally anisotropic media. This study is a response to several recent magnetotelluric interpretation attempts which have taken seriously the possibility of large electrical anisotropies within crustal and upper mantle geoelectrical structures.

As regards the theoretical formulation of the problem, there

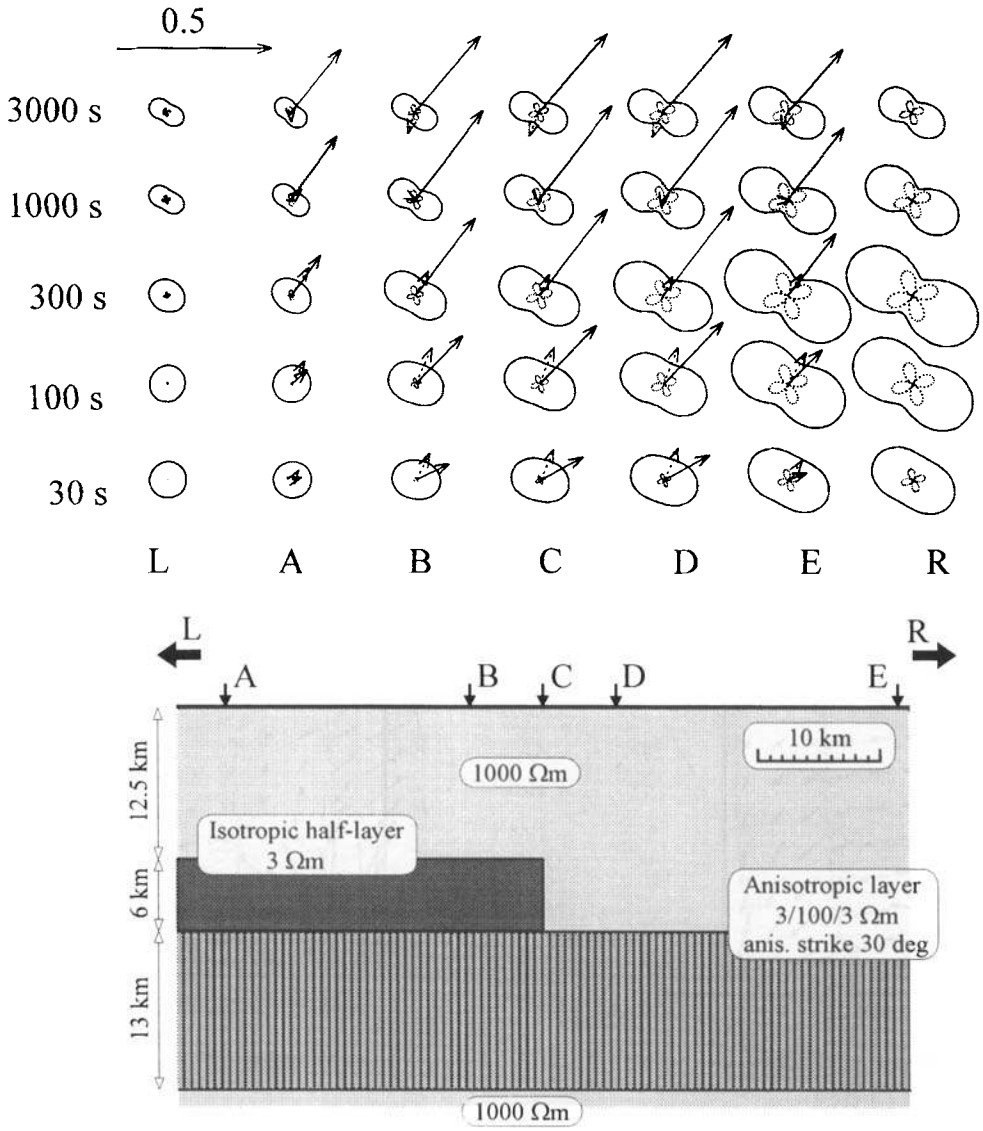

Figure 8. Top view of the real (full arrows) and imaginary (dashed arrows) induction arrows and polar impedance diagrams for a model with a lateral conductivity contact placed above an anisotropic layer. The conductivity tensor of the anisotropic layer is given by the principal resistivities $\rho_{\xi\xi}/\rho_{\eta\eta}/\rho_{zz} = 3/100/3\ \Omega$ m and the anisotropy strike of 30° towards R. All resistivities are in Ω m. The normalization of the polar impedance diagrams is the same as in Fig. 5.

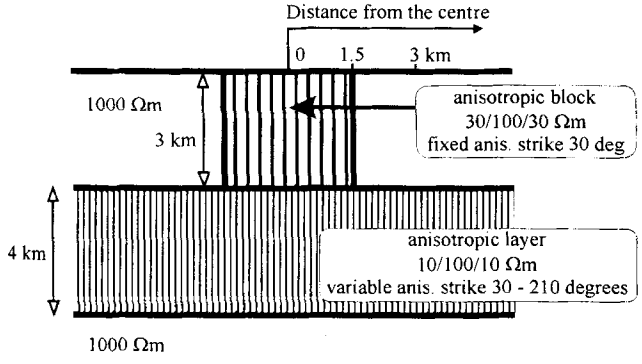

Figure 9. Model of an outcropping anisotropic block underlain by an anisotropic layer with a different anisotropy strike.

has not been too much progress when Reddy & Rankin (1975) is taken as a reference basis. Their analysis of a slightly less general problem with only the anisotropy strike considered already revealed the mechanism of mode-mixing in anisotropic structures. Additional degrees of freedom for the conductivity tensor, given by allowing for the anisotropy dip and slant, generalize the principal field equations (9) and (10) only by extending eq. (10) by the mixed derivatives second-order terms. The inter-mode coupling is not affected substantially by this extension.

The numerical solution of the problem is based on the FD approximation of the mutually coupled field equations (9) and (10) by using the integral form of Maxwell's equations in the close vicinity of each grid node. Two specific features of the algorithm may be worth mentioning: (i) the conductivity tensor within each of the anisotropic subdomains of the medium can be represented by an arbitrary symmetric, positive-definite matrix, thus allowing the anisotropy strike, dip, and slant to be introduced; and (ii) under the quasi-steady state conditions, the H-mode equations need not be

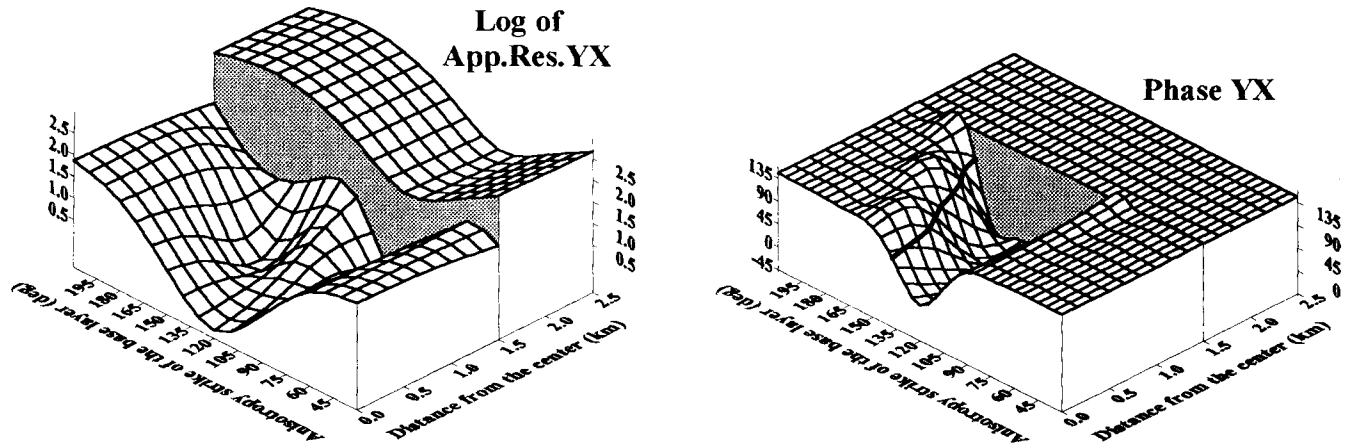

Figure 10. Surface plots of the apparent resistivity ρ^a_{yx} and phase ϕ_{yx} for the model from Fig. 9 as a function of the distance from the centre of the model for various anisotropy strikes of the base layer.

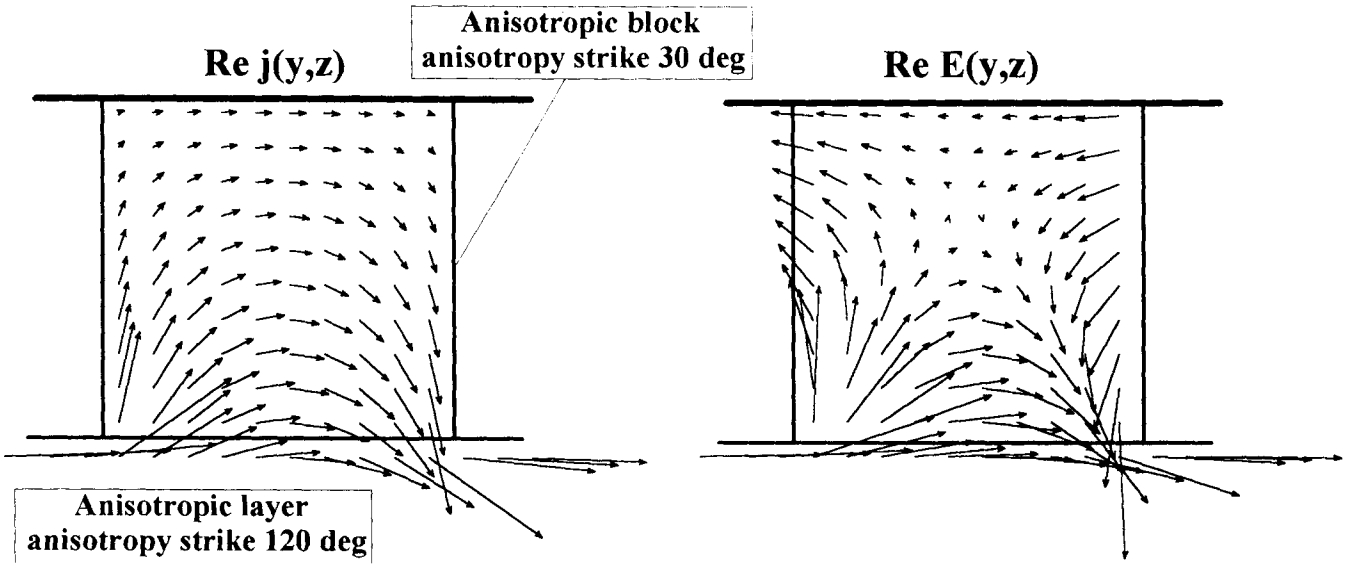

Figure 11. Vertical projections of the current density and the electric intensity in the anisotropic block from the model in Fig. 9. The difference between the anisotropy strikes of the outcrop and the base layer is 90°. The generating primary magnetic field is $H_{0x} = -1$, $H_{0y} = 0$. The period of the field is 30 s.

approximated within the non-conductive air layer, which allows us to avoid numerical difficulties arising from the huge conductivity contrasts at the earth–air interface, as well as to reduce slightly the size of the problem. As for the computational demands, for models of not too extreme a size the system of the approximate FD equations can be solved by Gaussian elimination in a reasonable time and with acceptable memory requirements on a PC.

The algorithm is written in an elementary form, without any refinements, such as asymptotic boundary conditions at infinity, integral boundary conditions on the surface of the conductive earth, or refined formulae for the spatial derivatives as proposed by Weaver, Le Quang & Fischer (1985, 1986), etc., which are often encountered in routine 2-D 'isotropic' modelling codes. Some of those procedures can become rather intricate when general anisotropy is involved.

With the numerical examples chosen for demonstration we tried to show that models containing anisotropic structures can produce data with qualitative features that are unknown in isotropic media. The most striking phenomena are generally connected with the strike-parallel component of the electric intensity arising from the deflection, owing to the anisotropy, of strike-perpendicular currents.

In particular, azimuths of the real induction arrows, which are commonly considered to represent an undistorted strike indicator, can be severely affected by large-scale anisotropic structures within the geoelectrical section. The deflection of the induction arrows with respect to the structural strike is largely dependent on whether the anisotropic sub-domain is itself the primary source of the vertical magnetic field, or whether it exerts a secondary influence on the vertical magnetic component generated elsewhere in the structure. The deflection of the induction arrows may be in quite opposite directions in the above two cases, which might cause confusion when interpreting the structural and anisotropy strikes of the medium.

The other example presented changes the common view on static-shift manifestations if anisotropic structures are located

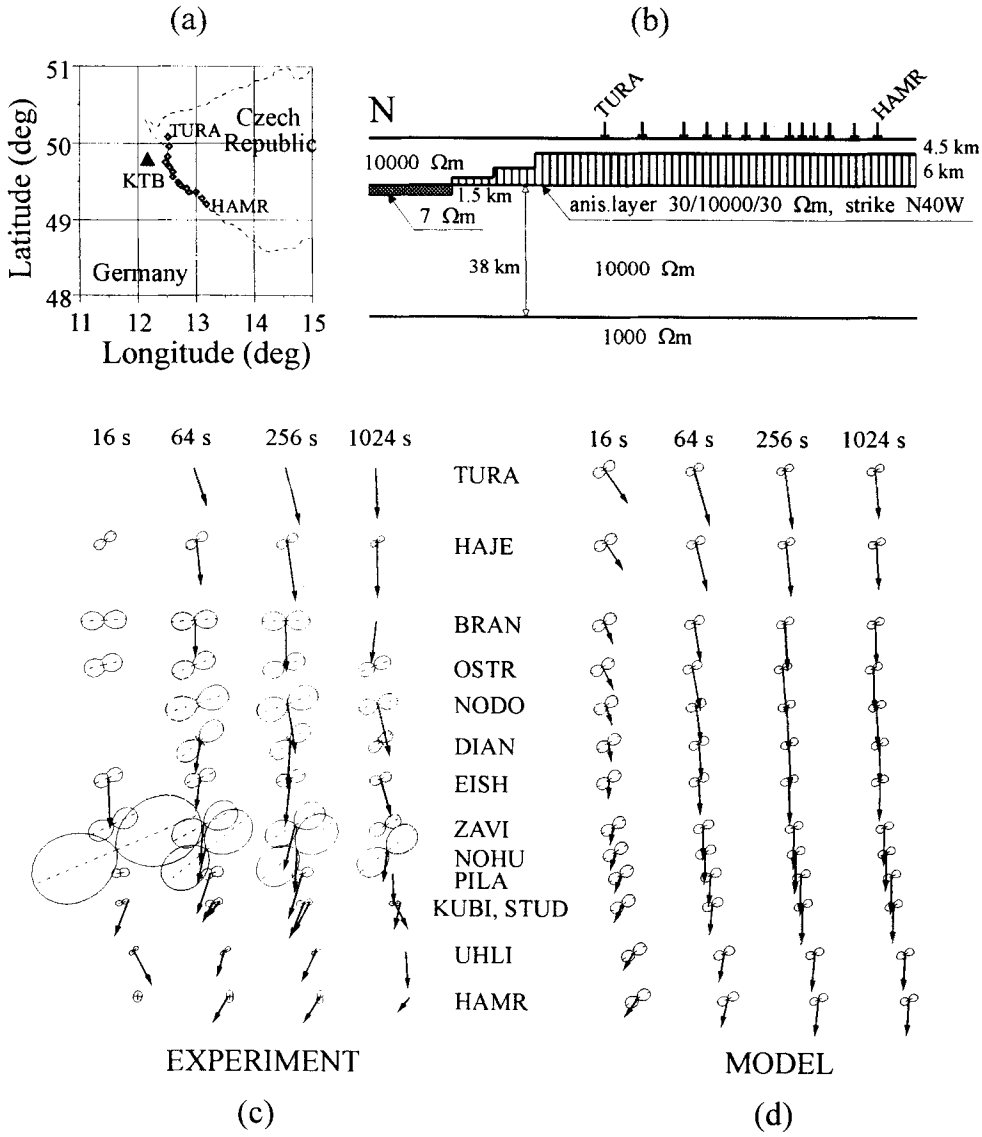

Figure 12. A speculative schematic model of a crustal anisotropic structure beneath the western part of the Bohemian Massif (Czech Republic). (a) Layout of the magnetotelluric stations along the Czech–German border, and the location of the deep drilling experiment KTB (Germany). (b) N–S section of the geoelectrical model with a highly conductive half-layer in the N and a largely anisotropic layer in the upper crust beneath the profile. (c) Experimental real induction arrows and main polar impedance diagrams at individual stations along the profile for four periods of the field. (d) Corresponding modelling results obtained for the model from (b). To avoid scaling difficulties, all impedances are reduced by the square root of the period.

in the distorting surface layer. As opposed to the isotropic case, at outcropping contacts of anisotropic bodies a discontinuity of both the 'perpendicular' apparent resistivities and phases is observed. Moreover, largely anisotropic composite structures seem to be able to blur the common concept of principal (antidiagonal) and secondary (diagonal) impedances as known from isotropic 2-D situations.

The examples presented were chosen rather arbitrarily, and do not cover the subject of anisotropy effects systematically. Nevertheless, they clearly demonstrate that severe distortions of magnetotelluric functions can occur if it is accepted that large anisotropies exist within the Earth.

The electrical macro-anisotropy in the Earth is generally a bulk property, which mostly results from a specific arrangement of the conductive fraction within the structures due to geodynamical, thermodynamical, or geochemical processes. Therefore, models with intrinsic anisotropy are necessarily only an approximation of the natural conditions, and we consider it important for further studies to clarify how far the analogy between the intrinsic anisotropy and the bulk anisotropy can be followed, especially as regards their influence on the observable geoelectrical data.

ACKNOWLEDGMENTS

We would like to thank Dr Václav Červ for his many helpful suggestions, particularly on the numerical part of the work. The research was supported by the Grant Agency of the Czech Republic under grant No. 205/93/0409 to the Geophysical Institute of the Academy of Sciences of the Czech Republic.

REFERENCES

Brewitt-Taylor, C.R. & Weaver, J.T., 1976. On the finite difference solution of two-dimensional induction problems, *Geophys. J. R. astr. Soc.*, **47,** 375–396.

Červ, V. & Praus, O., 1978. Numerical modelling in laterally inhomogeneous geoelectrical structures, *Studia Geophys. et Geodaet.*, **22,** 72–81.

Červ, V., Pek, J., Pěčová, J. & Praus, O., 1993. Electromagnetic measurements in the vicinity of the KTB drill site. Part II: Magnetotelluric results, *Studia Geophys. et Geodaet.*, **37,** 168–188.

Červ, V., Pek, J. & Praus, O., 1994. Magnetotelluric and magnetovariational measurements in Southwest Bohemia, data presentation and modelling experiments, in *Proc. Colloq. Electromagnetic Deep Investigations,* pp. 238–249, eds Bahr, K. & Junge, A., German Geophysical Society, Potsdam.

d'Erceville, I. & Kunetz, G., 1962. The effect of fault on the earth's natural electromagnetic field, *Geophysics,* **27,** 651-665.

Eisel, M., 1994. An anisotropic model of the ZEV, in *Proc. Colloq. Electromagnetic Deep Investigations,* pp. 40–46, eds Bahr, K. & Junge, A. German Geophysical Society, Potsdam (in German).

Eisel, M. & Bahr, K., 1993. Electrical anisotropy in the lower crust of British Columbia: an interpretation of a magnetotelluric profile after tensor decomposition, *J. Geomag. Geoelectr.*, **45,** 1115–1126.

Grubert, D., 1994. An extension of the classical solution from d'Erceville & Kunetz to anisotropic resistivity, *poster presented at 12th Workshop on Electromagnetic Induction in the Earth,* abstract No. P. 7a–16, IAGA, Brest.

Haak, V., 1972. Magnetotellurics: Determination of the transfer functions in regions with lateral changes of the electrical conductivity, *Z. Geophys.*, **38,** 85–102 (in German).

Jones, A.G., Groom, R.W. & Kurtz, R.D., 1993. Decomposition and modelling of the BC87 dataset, *J. Geomag. Geoelectr.*, **45,**1127–1150.

Kurtz, R.D., Mareschal, M., Niblett, E.R. & Kurtz, R.D., 1993. The conductivity of the crust and mantle beneath the Kapuskasing Uplift: electrical anisotropy in the upper mantle, *Geophys. J. Int.*, **113,** 483–498.

Loewenthal, D. & Landisman, M., 1973. Theory for magnetotelluric observations on the surface of a layered anisotropic half space, *Geophys. J. R. astr. Soc.*, **35,** 195–214.

Mackie, R.L., Madden, T.R. & Wannamaker, P.E., 1993. Three-dimensional magnetotelluric modelling using difference equations —Theory and comparisons to integral equation solutions, *Geophysics,* **58,** 215–226.

Osella, A.M. & Martinelli, P., 1993. Magnetotelluric response of anisotropic 2-D structures, *Geophys. J. Int.*, **115,** 819–828.

Reddy, I.K. & Rankin, D., 1971. Magnetotelluric effect of dipping anisotropies, *Geophys. Prospect,* **19,** 84–97.

Reddy, I.K. & Rankin, D., 1975. Magnetotelluric response of laterally inhomogeneous and anisotropic structure, *Geophysics,* **40,** 1035–1045.

Saraf, P.D., Negi, J.G. & Červ, V., 1986. Magnetotelluric response of a laterally inhomogeneous anisotropic inclusion, *Phys. Earth planet. Inter.*, **43,** 196–198.

Schmucker, U., 1994a. 2-D model computations of the induction in inhomogeneous thin sheets above anisotropic layered half-spaces, in *Proc. Colloq. Electromagnetic Deep Investigations,* pp. 3–26, eds Bahr, K. & Junge, A., German Geophysical Society, Potsdam (in German).

Schmucker, U., 1994b. Non-uniform thin sheets above a layered anisotropic halfspace, *poster presented at 12th Workshop on Electromagnetic Induction in the Earth,* abstract No. P. 7b-13, IAGA, Brest.

Stoll, J., 1989. Measurements of the natural electric potentials close to steeply dipping conductive structures and their geophysical interpretation, *Diploma thesis,* Inst. of Meteorology and Geophysics, University of Frankfurt (in German).

Tauber, S., 1993. The conductivity distribution in the northern Variscides investigated by the magnetotelluric and geomagnetic deep sounding method along a profile from the Oberpfälzer Wald to Vogtland, *Diploma thesis,* Inst. of Geol., Geoph. und Geoinform., Free University of Berlin (in German).

Tezkan, B., 1988. An interpretation attempt to explain the contrary course of the E and B polarization phases at the eastern margin of the Hessische Senke by using two-dimensional conductivity models, in *Proc. Colloq. Electromagnetic Deep Investigations,* pp. 35–54, eds Haak, V. & Homilius, J., Niedersächsisches Landesamt für Bodenforschung, Hannover (in German).

Tezkan, B., Červ, V. & Pek, J., 1992. Resolution of anisotropic and shielded highly conductive layers using 2-D electromagnetic modelling in the Rhine Graben and Black Forest, *Phys. Earth planet. Inter.*, **74,** 159–172.

Weaver, J.T., Le Quang, B.V. & Fischer, G., 1985. A comparison of analytical and numerical results for a two dimensional control model in electromagnetic induction. I. B-polarization calculations, *Geophys. J. R. astr. Soc.*, **82,** 263–277.

Weaver, J.T., Le Quang, B.V. & Fischer, G., 1986. A comparison of analytical and numerical results for a two dimensional control model in electromagnetic induction. I. E-polarization calculations, *Geophys. J. R. astr. Soc.*, **87,** 917–948.

Weidelt, P., 1994. FD-Modelling of 3-D structures with arbitrary anisotropic conductivity, *poster presented at 12th Workshop on Electromagnetic Induction in the Earth,* abstract No. P. 7a–19, IAGA, Brest.

Winter, H., 1994. Electrical conductivity in the KTB—Comparison of laboratory and in-situ measurements, in *Proc. Colloq. Electromagnetic Deep Investigations,* pp. 346–353, eds Bahr, K. & Junge, A., German Geophysical Society, Potsdam (in German).

Xiong, Z., 1989. Electromagnetic fields of electric dipoles embedded in a stratified anisotropic earth, *Geophysics,* **54,** 1643–1646.

Yudin, M.N., 1982. Algorithm of selection of net parameters in calculations of magnetotelluric field by the finite-difference method, in *Geomagnetic Researches,* No. 29, pp. 91–95, eds Vanyan, L.L., Debabov, A.S. & Kharin, J.P., Radio i Svyaz, Moscow (in Russian).

APPENDIX A: FD SCHEMES FOR THE 2-D MODELLING IN ANISOTROPIC STRUCTURES

In this Appendix, the finite difference schemes and coefficients are summarized which arise from FD approximating the basic differential equations (9) and (10). The schemes display eight points which surround the (j, k)th grid node along with the corresponding coefficients $C^{EE}_{jk}(p, q)$, $C^{EH}_{jk}(p, q)$, $C^{HE}_{jk}(p, q)$, and $C^{HH}_{jk}(p, q)$, $p \in \{j-1, j, j+1\}$, $q \in \{k-1, k, k+1\}$ [see eqs (13), (16)]. For each point in the scheme, the coefficients for the electric component, E_x, are given in the top half-box, and those for the magnetic field, H_x, in the bottom half-box.

A1: E-mode equation [eqs (9), (13)]

$$P^E_{j,k} = (\Delta z_k + \Delta z_{k+1})/(2\Delta y_j), \qquad Q^E_{j,k} = (\Delta y_j + \Delta y_{j+1})/(2\Delta z_k),$$

$$R^E_{j,k} = (\Delta y_j + \Delta y_{j+1})/(2\Delta z_{k+1}),$$

$$S^E_{j,k} = (\Delta z_k + \Delta z_{k+1})/(2\Delta y_{j+1}),$$

$$V^E_{j,k} = -(P^E_{j,k} + Q^E_{j,k} + R^E_{j,k} + S^E_{j,k}),$$

$$T^E_{j,k} = \frac{1}{4}\omega\mu_0 \sum_{p=j}^{j+1} \sum_{q=k}^{k+1} (\sigma_{xx} + A\,\sigma_{zx} + B\,\sigma_{yx})_{p,q}\,\Delta y_p\,\Delta z_q,$$

$$X^{E,L}_{j,k} = \Delta z_k A_{j,k} + \Delta z_{k+1} A_{j,k+1}\,,$$
$$X^{E,R}_{j,k} = \Delta z_k A_{j+1,k} + \Delta z_{k+1} A_{j+1,k+1}\,,$$
$$X^{E,U}_{j,k} = \Delta y_j B_{j,k} + \Delta y_{j+1} B_{j+1,k}\,,$$
$$X^{E,D}_{j,k} = \Delta y_j B_{j,k+1} + \Delta y_{j+1} B_{j+1,k+1}\,,$$
$$X^{E}_{j,k} = X^{E,L}_{j,k} - X^{E,U}_{j,k} + X^{E,D}_{j,k} - X^{E,R}_{j,k}\,.$$

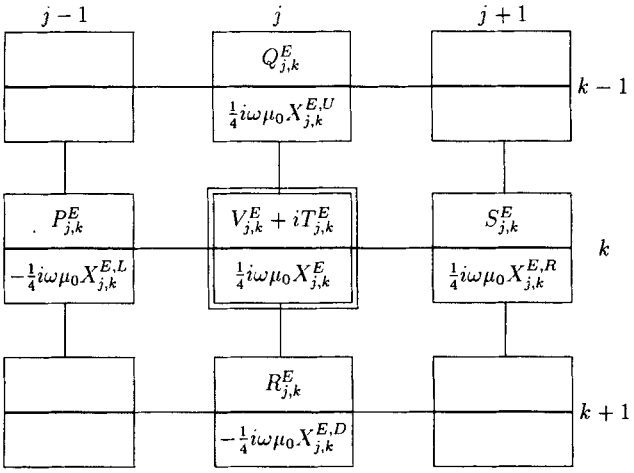

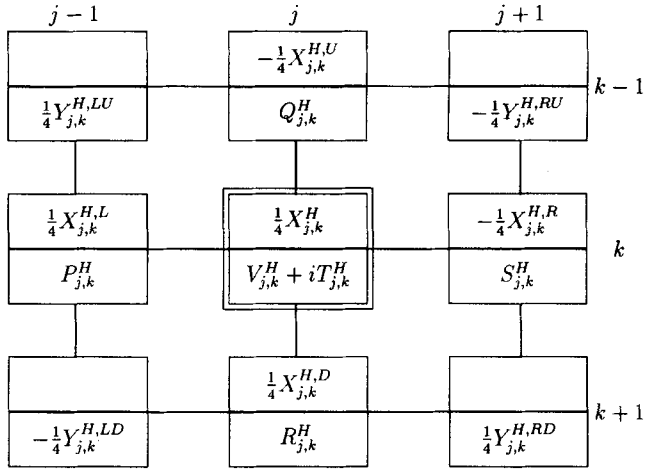

A2: H-mode equation [eqs (10), (16)]

$$P^H_{j,k} = [\Delta z_k\,(\sigma_{yy}/D)_{j,k} + \Delta z_{k+1}\,(\sigma_{yy}/D)_{j,k+1}]/(2\Delta y_j)\,,$$
$$Q^H_{j,k} = [\Delta y_j\,(\sigma_{zz}/D)_{j,k} + \Delta y_{j+1}\,(\sigma_{zz}/D)_{j+1,k}]/(2\Delta z_k)\,,$$
$$R^H_{j,k} = [\Delta y_j\,(\sigma_{zz}/D)_{j,k+1} + \Delta y_{j+1}\,(\sigma_{zz}/D)_{j+1,k+1}]/(2\Delta z_{k+1})\,,$$
$$S^H_{j,k} = [\Delta z_k\,(\sigma_{yy}/D)_{j+1,k} + \Delta z_{k+1}\,(\sigma_{yy}/D)_{j+1,k+1}]/(2\Delta y_{j+1})\,,$$
$$V^H_{j,k} = -(P^H_{j,k} + Q^H_{j,k} + R^H_{j,k} + S^H_{j,k}) - \frac{1}{4}(Y^{H,LU}_{j,k} - Y^{H,RU}_{j,k} + Y^{H,LD}_{j,k} - Y^{H,RD}_{j,k})\,,$$
$$T^H_{j,k} = \frac{1}{4}\omega\mu_0(\Delta y_j + \Delta y_{j+1})(\Delta z_k + \Delta z_{k+1})\,,$$
$$X^{H,L}_{j,k} = \Delta z_k B_{j,k} + \Delta z_{k+1} B_{j,k+1}\,,$$
$$X^{H,R}_{j,k} = \Delta z_k B_{j+1,k} + \Delta z_{k+1} B_{j+1,k+1}\,,$$
$$X^{H,U}_{j,k} = \Delta y_j A_{j,k} + \Delta y_{j+1} A_{j+1,k}\,,$$
$$X^{H,D}_{j,k} = \Delta y_j A_{j,k+1} + \Delta y_{j+1} A_{j+1,k+1}\,,$$
$$X^{H}_{j,k} = X^{H,L}_{j,k} - X^{H,U}_{j,k} + X^{H,D}_{j,k} + X^{H,R}_{j,k}$$
$$Y^{H,LU}_{j,k} = 2(\sigma_{yz}/D)_{j,k}\,, \qquad Y^{H,RU}_{j,k} = 2(\sigma_{yz}/D)_{j+1,k}\,,$$
$$Y^{H,LD}_{j,k} = 2(\sigma_{yz}/D)_{j,k+1}\,, \qquad Y^{H,RD}_{j,k} = 2(\sigma_{yz}/D)_{j+1,k+1}\,.$$